Anisotropic interactions opposing magnetocrystalline anisotropy in Sr_3NiIrO_6

E. Lefrançois,[1,2,3,*] A.-M. Pradipto,[4,†] M. Moretti Sala,[5] L. C. Chapon,[1] V. Simonet,[2,3] S. Picozzi,[4] P. Lejay,[2,3] S. Petit,[6] and R. Ballou[2,3]

[1]*Institut Laue Langevin, CS 20156, 38042 Grenoble Cedex 9, France*
[2]*CNRS, Institut Néel, 38042 Grenoble, France*
[3]*Université Grenoble Alpes, Institut Néel, 38042 Grenoble, France*
[4]*Consiglio Nazionale delle Ricerche, CNR-SPIN, L'Aquila, Italy*
[5]*European Synchrotron Radiation Facility, CS 40220, 38043 Grenoble Cedex 9, France*
[6]*Laboratoire Léon Brillouin, CEA, CNRS, Université Paris Saclay, CEA Saclay, F-91191 Gif-sur-Yvette, France*

(Received 21 April 2015; revised manuscript received 13 April 2016; published 1 June 2016)

We report our investigation of the electronic and magnetic excitations of Sr_3NiIrO_6 by resonant inelastic x-ray scattering at the Ir L_3 edge. The intra-t_{2g} electronic transitions are analyzed using an atomic model, including spin-orbit coupling and trigonal distortion of the IrO_6 octahedron, confronted with *ab initio* quantum chemistry calculations. The Ir spin-orbital entanglement is quantified and its implications for the magnetic properties, in particular in inducing highly anisotropic magnetic interactions, are highlighted. These are included in the spin-wave model proposed to account for the dispersionless magnetic excitation that we observe at 90 meV. By counterbalancing the strong Ni^{2+} easy-plane anisotropy that manifests itself at high temperature, the anisotropy of the interactions finally leads to the remarkable easy-axis magnetism reported in this material at low temperature.

DOI: 10.1103/PhysRevB.93.224401

Since the discovery of spin-orbit-induced Mott insulator in Sr_2IrO_4 [1], it has become apparent that electron correlation effects can be important in 5*d* transition metal oxides when combined with spin-orbit coupling (SOC), despite rather wide *d* electronic bands. In a perfect octahedral environment of $5d^5$ low-spin systems, e.g., in Ir^{4+} oxide compounds, SOC splits the t_{2g} band occupied by the 5 electrons into a fully occupied $j_{\text{eff}} = \frac{3}{2}$ band and a narrow singly occupied $j_{\text{eff}} = \frac{1}{2}$ band. This band can be gapped by a fair amount of Hubbard repulsion driving the system toward an insulating state. This can persist even when the ideal $j_{\text{eff}} = \frac{1}{2}$ state is not realized, i.e., when it is mixed with the $j_{\text{eff}} = \frac{3}{2}$ states due to the Ir^{4+} nonregular octahedral environment [see Fig. 1(b)], as is generally the case in the known iridates [2–5]. The influence of SOC is not limited to transport properties. Another very interesting perspective in the field of iridates is the strong anisotropy of the magnetic interactions produced by spin-orbital entanglement. This is expected to give rise to novel exotic magnetic states and excitations, still to be discovered [6,7].

In this context, the compounds of the family $A_3MM'O_6$ (A = alkaline-earth metal, M, M' = transition metal) are of interest because the M' site can be occupied by Ir^{4+}. Most members of the family crystallize in the K_4CdCl_6-derived rhombohedral structure in which alternating distorted trigonal prismatic MO_6 and nearly octahedral $M'O_6$ coordinations constitute chains along the rhombohedral axis (see Fig. 3) arranged on a triangular lattice. They show complex magnetic behaviors attributed mainly to frustration and low dimensionality, enhanced by strong magnetocrystalline anisotropy and the presence of two magnetic species. Sr_3NiIrO_6 displays particularly intriguing properties: a complex antiferromagnetic structure below a Néel temperature T_N of 70 K with slow spin dynamics and two consecutive correlated magnetic regimes when lowering the temperature [8–11]. The ordered magnetic moments are aligned along the *c* axis, but there is currently no explanation for the origin of the large anisotropy (single-ion effect or exchange-driven mechanism) and its relation with the very high coercive field [12] of this material. The role played by SOC and anisotropic exchange is therefore a key issue. Three groups have performed *ab initio* electronic structure calculations [13–15] confirming the Sr_3NiIrO_6 Mott-insulating state. Nevertheless, they disagree about the nature of the frontiers 5*d* electronic levels, the sign of the nearest-neighbor Ni-Ir interactions, and the magnetocrystalline anisotropy. The role of SOC has been investigated in the related Cu compound by resonant inelastic x-ray scattering (RIXS) [16,17]. However, the distortion of the Ir^{4+} octahedral environment in Sr_3CuIrO_6 is monoclinic, which leads to nonequivalent Ir-O distances and O-Ir-O angles. The resulting $j_{\text{eff}} = \frac{1}{2}$ and $j_{\text{eff}} = \frac{3}{2}$ mixed states and their overlap with the Cu 3*d* orbitals are then at the origin of an unusual ferromagnetic exchange anisotropy arising from antiferromagnetic superexchange [17]. Ir^{4+} octahedra in Sr_3NiIrO_6, instead, only experience a pure elongation along the trigonal *c* axis, which preserves equivalent Ir-O distances. Sr_3NiIrO_6 is accordingly a nice candidate to study the influence of simple distortion on the electronic and magnetic properties.

Hereafter, we report RIXS experiment on Sr_3NiIrO_6 probing simultaneously its electronic and magnetic excitations. The local atomic effective Hamiltonian of Sr_3NiIrO_6 is derived, complemented by quantum chemistry *ab initio* calculations. The analysis of the magnetic excitations reveals a large Ising anisotropy in the Ni-Ir magnetic exchange which competes with a sizable single-ion planar anisotropy for the Ni ions. This competition explains the directional crossover of the magnetization observed at high temperature.

RIXS measurements were performed at the ID20 beam line of the European Synchrotron Radiation Facility. The beam line is equipped with a 2 m arm spectrometer, based on spherical Si(844) diced crystal analyzers. The combination of

*Corresponding author: lefrancois@ill.fr
†Corresponding author: a.m.t.pradipto@gmail.com

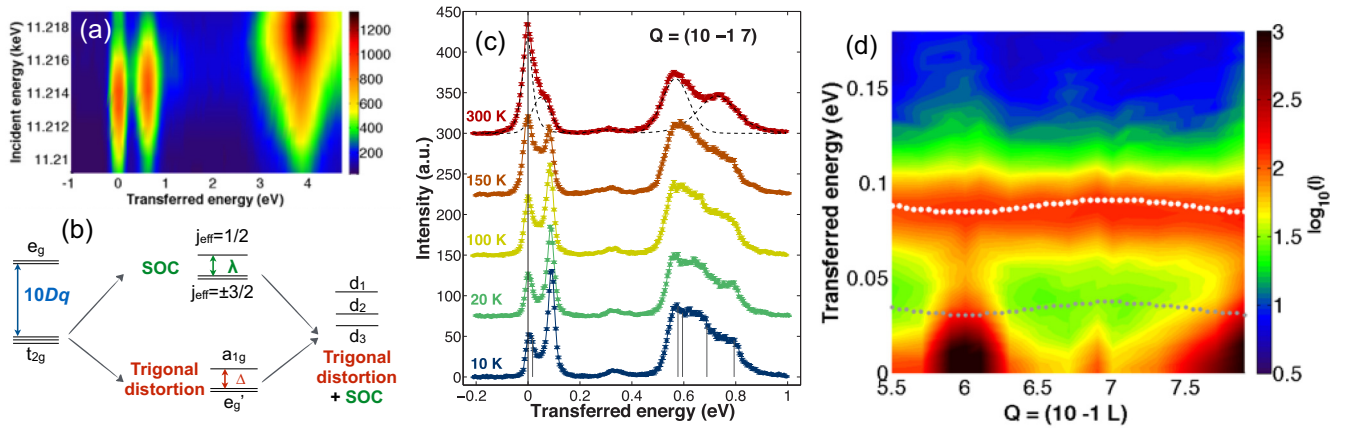

FIG. 1. (a) Incident energy dependence of the Sr_3NiIrO_6 RIXS spectra at the L_3 Ir edge measured at 300 K, showing the resonance of the t_{2g} and e_g levels. (b) Splitting of the $5d$ levels due to the octahedral environment ($10Dq$), to its trigonal distortion, and to SOC. (c) RIXS spectra at the reciprocal space position $\mathbf{Q} = (10\text{–}1\ 7)$ between 10 and 300 K. The scans are offset by 75 counts for clarity. The dashed curves on the 300 K data correspond to least-squares refinements of the excitations using Pearson-VII functions. The vertical lines on the 10 K curve correspond to the eigenvalues of $\mathcal{H}$ calculated for $\lambda = 396$ meV, $\Delta = 294$ meV, $\alpha_{x,y} = 0$, and $\alpha_z = 0.1$ eV. (d) RIXS map measured at 10 K along the (10–1 L) direction. The dotted lines show the spin-wave excitations calculated with $J_{xx} = J_{yy} = 20$ meV, $J_{zz} = 46$ meV, and $D = 9$ meV. The Ir and Ni main contributions are in white and gray, respectively.

the Si(111) double-crystal monochromator with a channel cut allows for a flexible choice of the energy resolution down to 25 meV [18] at the Ir L_3 edge. RIXS has proven an ideal tool in the study of the iridate electronic structure [3,16,19,20], as it directly probes $5d$ states via two successive dipole transitions [21,22]. Measurements were performed between 300 and 10 K on a single crystal of Sr_3NiIrO_6, grown using the flux method [11]. Figure 1(a) shows a RIXS map obtained from inelastic scans at different incident photon energies. The resonance of the Ir^{4+} electronic levels is observed at 11.214 keV for the t_{2g} and at 11.218 keV for the e_g. For all measurements presented below, the incident photon energy was fixed to 11.214 keV, which enhances the excitations within the t_{2g} manifold.

The RIXS spectra of Sr_3NiIrO_6 measured at the momentum transfer $\mathbf{Q} = (10\text{–}1\ 7)$ of a forbidden Bragg peak position are shown Fig. 1(c). We first focus on the room temperature measurement where four features are visible beside the elastic peak, at the energies of 50(5), 322(20), 568(2), and 728(5) meV, none of them showing any detectable dispersion within the lowest instrumental resolution. The most intense peaks at 568(2) and 728(5) meV are interpreted as d-d excitations within the t_{2g} levels [4,16,17], i.e., as transitions of the hole from the ground state to the two lower lying filled states [see Fig. 1(b)]. In addition to the SOC splitting of the t_{2g}, a trigonal crystal field indeed further splits the $j_{\text{eff}} = \frac{3}{2}$ ground manifold. This effect can be quantified using a local atomic model for the single hole in the $^2T_{2g}$ states with the Hamiltonian

$$\mathcal{H} = \Delta\left(\frac{2}{3}|a_{1g}\rangle\langle a_{1g}| - \frac{1}{3}|e_g'^{\pm}\rangle\langle e_g'^{\pm}|\right) + \lambda\mathbf{L}\cdot\mathbf{S} - \sum_{i\in x,y,z}\alpha_i S_i, \tag{1}$$

where Δ describes the t_{2g} orbitals splitting due to the IrO_6 octahedron trigonal distortion ($\Delta > 0$ for an axial elongation) and λ is the SOC parameter. The symmetry-adapted $|a_{1g}\rangle$ and $|e_g'^{\pm}\rangle$ wave functions for trigonal symmetry are defined in the Supplemental Material [23]. The $10Dq$ splitting between t_{2g} and e_g levels is of the order of 4 eV [see Fig. 1(a)], i.e., much larger than λ and Δ, and therefore the e_g levels can safely be ignored. The last terms, $\alpha_i S_i = -2J_{ii}\langle S_i^{\text{Ni}}\rangle S_i$ ($i = x,y,z$), are the molecular field components produced on the Ir spin by its two Ni^{2+} nearest neighbors. For the analysis of the 300 K data, far above T_N, we first assume $\alpha_{x,y,z} = 0$, i.e., weak influence of the magnetic interactions.

The values of λ and Δ are obtained by constraining the eigenvalues of $\mathcal{H}$ to the energies of the t_{2g} manifold excitations determined from the experiment. Two solutions exist, depending on the sign of Δ: $\lambda = 396(1)$ meV and $\Delta = 294(7)$ meV for the first one and $\lambda = 417(4)$ meV and $\Delta = -218(8)$ meV for the second one. The wave functions (shown in Fig. 2) for the highest doublet in the $^2T_{2g}$ subspace (occupied by the hole) are

$$|0,\uparrow\rangle = \frac{ip|a_{1g},\uparrow\rangle + i|e_g'^{+},\downarrow\rangle + |e_g'^{-},\downarrow\rangle}{\sqrt{p^2+2}},$$
$$|0,\downarrow\rangle = \frac{p|a_{1g},\downarrow\rangle - |e_g'^{+},\uparrow\rangle - i|e_g'^{-},\uparrow\rangle}{\sqrt{p^2+2}}, \tag{2}$$

with the evolution of p with Δ/λ shown in Fig. 2. The sign of Δ cannot be determined by the RIXS analysis alone. However, the Ir magnetic moment refined in neutron diffraction [11] seems in better agreement with the z component of the total magnetic moment, $\langle L_z + 2S_z\rangle$, calculated for a positive Δ ($0.25\,\mu_B$) than for a negative one ($1.35\,\mu_B$), as shown in Fig. 2. Nevertheless, a strong reduction of the magnetic moment by quantum fluctuations, enhanced by low dimensionality or geometric frustration, is not excluded.

Another argument in favor of $\Delta > 0$ comes from *ab initio* calculations. For these, we used a quantum chemistry inherited computational scheme [3,4,16,24], in which it was shown

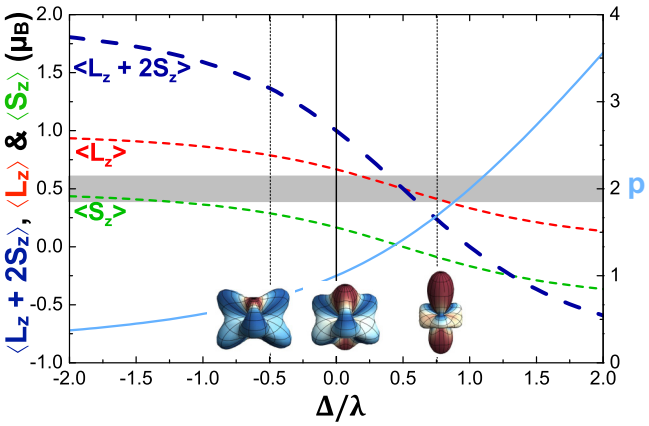

FIG. 2. Evolution of the z components of the orbital $\langle L_z\rangle$, spin $\langle S_z\rangle$, total magnetic moment $\langle L_z + 2S_z\rangle$, and p as a function of $\frac{\Delta}{\lambda}$. The gray stripe shows the Ir magnetic moment refined from neutron diffraction [11]. The amplitudes of the probability of presence of the t_{2g} hole are shown at the bottom: for a perfect octahedral environment ($\frac{\Delta}{\lambda} = 0$), for a trigonal compression ($\frac{\Delta}{\lambda} = -0.52$), and for a trigonal elongation ($\frac{\Delta}{\lambda} = 0.73$) of the octahedron. The latter two are in agreement with the RIXS results but only the positive $\frac{\Delta}{\lambda}$ is compatible with quantum chemistry calculations. The surfaces of constant amplitude of probability are colored from red for pure $|a_{1g},\uparrow\rangle$ state, to blue for pure $(i|e_g'^{+},\downarrow\rangle + |e_g'^{-},\downarrow\rangle)$ state, through white for an equal mix of these states.

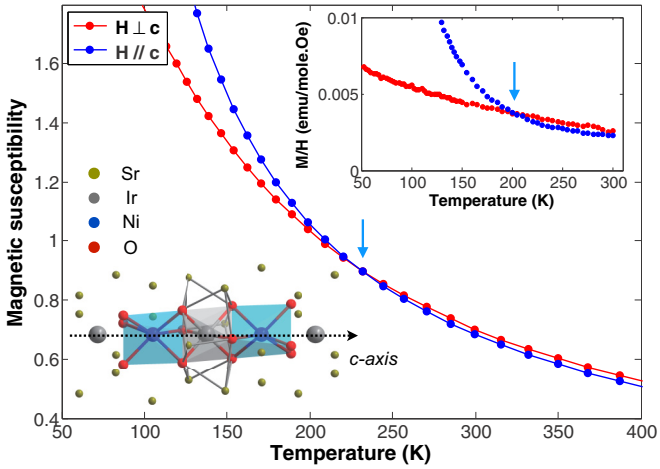

FIG. 3. Magnetic susceptibility of Sr_3NiIrO_6 calculated by Monte Carlo simulation using the spin-wave parameters. The blue (red) curve is obtained for the magnetic field applied along (perpendicular to) the chain direction. Top inset: Comparison with the measurements reported in Ref. [11]. The arrows indicate the crossing of the curves. Bottom inset: Detail of the Sr_3NiIrO_6 structure with the central distorted IrO_6 octahedron along the chain axis.

that the combination of the MultiReference Configuration Interaction method with SOC (MRCI+SOC) is able to reproduce the RIXS spectra. The local Ir-5d electronic structure has been investigated in the basis of multiconfigurational wave-function-based methods [23] which is implemented in the MOLCAS 7.8 code [25] to ensure a proper description of the multiplet physics.

The 54 spin-orbit Ni-Ir coupled states and their energies were calculated for the cluster shown in Fig. 3 [23]. In order to estimate the excitations only within the Ir-5d orbitals, we performed calculations by replacing the Ni^{2+} with nonmagnetic Zn^{2+}. Without SOC, we observe three doublet states, in which the degenerate $^2E_g'$ doublets lie 0.21 eV higher than the ground state (see Table I). This is in perfect agreement with the energy windows calculated with Ni^{2+}, confirming that these correspond to the excitation energies within the Ir-5t_{2g} manifold. Furthermore, the ground doublet state corresponds to the $d_1^1 d_2^2 d_3^2$ configuration, where d_1 is the a_{1g} orbital that can be written as d_{z^2}, while d_2 and d_3 correspond to the e_g' orbitals in the trigonal representation. One can hence conclude that the a_{1g} orbital lies higher in energy than the e_g' ones, in accordance with a positive Δ.

Taking into account the SOC, two excitations are calculated at 0.64 and 0.80 eV. These values are remarkably close to the energies found in the RIXS spectra, confirming that the associated peaks correspond to the splitting of the $j_{\text{eff}} = \frac{3}{2}$ quartet into two doublets. The weights of different t_{2g}^5 contributions to the spin-orbit coupled doublet states are shown in Table I. The ground state is not an equal mixture of the t_{2g} orbitals, the weight of $|\psi_1\rangle$ being larger than the other two degenerate configurations, with a ratio of 0.46 : 0.27 : 0.27 (to be compared with 0.33 : 0.33 : 0.33 in a perfect cubic environment). Overall, the room temperature RIXS measurements confronted to the *ab initio* calculations are fully consistent and allow us to describe quantitatively the electronic spectrum of the Ir^{4+} and its departure from the perfect $j_{\text{eff}} = \frac{1}{2}$ state due to its noncubic environment. An Ir-5t_{2g} orbital splitting Δ ranging between 0.21 and 0.30 eV is obtained, leading to a ratio $\Delta/\lambda \approx 0.53$–$0.74$ ($\lambda = 0.396$ eV estimated from RIXS). This scheme does not explain the weak signal observed at 322 meV. Its origin is unclear, but a feature with similar energy and spectral weight was reported in almost all the iridates [3,4,16], suggesting that it might be an intrinsic characteristics of this class of materials.

Lowering the temperature down to 10 K, the two intense peaks related to the t_{2g} electronic transitions change shape and acquire a substructure [see Fig. 1(c)]. This reflects the increasing influence, as the temperature decreases, of the Ni-Ir nearest-neighbor magnetic exchange interactions on the Ir electronic states. The molecular field produces a splitting of the peaks that can be calculated from the last term of Eq. (1).

TABLE I. SD-MRCI results for the t_{2g} level splittings (in eV) and weights of the different Ir-t_{2g} configurations. In the absence of SOC, $\epsilon_1 = \epsilon_2$ corresponds to the energy of the doubly degenerate E_g' state. The energies and weights extracted from the experiment for $\Delta > 0$ are shown in the last column.

	No SOC			With SOC			Exp. Values		
	ϵ_0	ϵ_1	ϵ_2	ϵ_0	ϵ_1	ϵ_2	ϵ_0	ϵ_1	ϵ_2
Configuration	0.00	0.21	0.21	0.00	0.64	0.80	0.00	0.57	0.73
$\lvert\psi_1\rangle = d_1^1 d_2^2 d_3^2$	1.00			0.46	0.54	0.00	0.58	0.42	0.00
$\lvert\psi_2\rangle = d_1^2 d_2^1 d_3^2$		1.00		0.27	0.23	0.50	0.21	0.29	0.50
$\lvert\psi_3\rangle = d_1^2 d_2^2 d_3^1$			1.00	0.27	0.23	0.50	0.21	0.29	0.50

Although the features observed in the range 500–900 meV do not allow us to univocally determine the values of $\alpha_{x,y,z}$, an example of splitting is shown on the 10 K spectrum of Fig. 1(c), in reasonable agreement with the experiment. It is obtained with $\alpha_{x,y} = 0$ and $\alpha_z = 0.1$ eV, agreeing with the strong uniaxial character of the magnetic structure, and with the value of the J_{zz} interaction determined hereafter.

At 300 K, the excitation at the lowest energy is broad with a position of the maximum at ≈50(5) meV. It rises in intensity while narrowing as the temperature is lowered [see Fig. 1(c)], and its energy rapidly shifts to ≈90(5) meV at 100 K, below which it remains constant. This excitation cannot be accounted for by the local electronic level scheme derived previously. It is attributed to a magnetic excitation whose observation by RIXS is allowed in this system [23]. The absence of any detectable dispersion is illustrated by the RIXS measurement along the (10–1 L) direction [see Fig. 1(d)]. Another magnetic excitation was identified at 35 meV by inelastic neutron scattering (INS) on a Sr_3NiIrO_6 powder sample [26]. It was also shown to persist up to 200 K, i.e., much above T_N, a behavior attributed to the presence of strong spin correlations associated with the low-dimensional nature of the magnetism. We succeeded in reproducing the spin-wave modes at 35 and 90 meV observed by INS and RIXS, respectively, using the Holstein-Primakov formalism within the linear approximation [see Fig. 1(d)] [23]. We used a simple model, in line with the reported magnetic structure [11,23], of isolated chains with (i) strong anisotropic antiferromagnetic exchange interactions between the nearest-neighbor Ni and Ir ions along the chain: $J_{xx} = J_{yy} =$ 20(2) meV, $J_{zz} = 46(2)$ meV, and (ii) magnetocrystalline anisotropy of the Ni^{2+} ions: DS_z^2 term with $D = 9(1)$ meV corresponding to an easy-plane single-ion anisotropy perpendicular to the chain axis. The effective interchain interaction was estimated from both the ordering temperature and the coercive field. It is more than one order of magnitude smaller than the intrachain interactions, affecting negligibly the spin excitations. It is furthermore irrelevant to the spin-wave dispersion along the chains. It can thus be safely ignored [23]. Extracting the ion-dependent neutron spectral weight of the excitations clearly demonstrates that Ir(Ni) mainly contributes to the high (low) mode [23]. This explains the absence of the INS 35 meV mode in the RIXS data since the measurements at the Ir L_3 edge are mainly sensitive to the resonant inelastic signal of Ir. Our model is highly constrained by the energies and dispersion of the modes extracted from the RIXS and INS data [23] and can uniquely account for the experimental results if one considers this easy-plane single-ion term. This term is a hallmark difference between the physics of Sr_3NiIrO_6 and Sr_3CuIrO_6, which otherwise shows rather similar anisotropic exchanges [17]. The strength of the exchange anisotropy is driven by p, which is related to the relative weight of the $|a_{1g}\rangle$ and $|e'_g\rangle$ wave functions in Eq. (2). Those are respectively preserving or not L_z when flipping S_z, hence contributing to the isotropic (resp. anisotropic) part of the interactions [17]. The parameter p varies with the octahedral distortion Δ and might be tunable by a chemical or external pressure.

To further support this model, it is found that the Ni anisotropy perfectly matches the one reported for the isostructural compound Sr_3NiPtO_6, for which $D \approx 9$ meV [27] and which is even considered as a prototypal example of a "large-D" system. Furthermore, the competition between strong exchange anisotropy (J_{zz}/J_{xx}) and single-ion anisotropy (DS_z^2) on the Ni site produces a hallmark feature in the magnetization measurement: at high temperature, the susceptibility measured for a magnetic field applied along the c direction is lower than the one obtained with a field in-plane. Below 200 K, the two curves cross due to the increasing influence of the large exchange anisotropy when correlations build up, ultimately leading to a uniaxial antiferromagnetic order. The directional crossover in the magnetic susceptibility is nicely reproduced by Monte Carlo simulations using a one-dimensional chain model and the parameters extracted from the spin-wave calculations (see Fig. 3) [23]. Finally, the large coercive field reported in Sr_3NiIrO_6 is simply explained as the minimum field responsible for the coherent reversal of the spin chains, its value agreeing with the interchain coupling [23].

To summarize, we have determined the 5d Ir electronic scheme in the Sr_3NiIrO_6 chain compound through our RIXS measurements and their analysis. The resulting spin-orbital-entangled ground state produces a strong anisotropy of the interactions, which is evidenced in our analysis of the spin-wave excitations including the two gapped modes seen by RIXS and neutron scattering. This uniaxial anisotropy of the interactions competes with a strong Ni^{2+} single-ion easy-plane anisotropy, a unique feature of this system in the series. Comparing our magnetic Hamiltonian to the one of a recent numerical study of a mixed-spin XXZ chain with single-ion anisotropy, it is found that, in the parameter space of exchange and single-ion anisotropies, Sr_3NiIrO_6 lies close to the boundary separating the observed ordered Ising ferrimagnetic phase from a disordered XY phase [28]. These results demonstrate the potential of SOC in triggering emerging physics. In mixed 3d-5d transition metal chain systems, it can allow us to probe unexplored regions of their phase diagram and quantum phase transitions.

We thank A. Al-Zein for this help during the RIXS experiment and A. Hadj-Azzem for his collaboration on the crystal synthesis. A.-M.P. and S.P. thank R. Broer for providing the computational facilities in the local computer cluster at the University of Groningen.

[1] B. J. Kim, H. Jin, S. J. Moon, J.-Y. Kim, B.-G. Park, C. S. Leem, J. Yu, T. W. Noh, C. Kim, S.-J. Oh *et al.*, Phys. Rev. Lett. **101**, 076402 (2008).

[2] M. Moretti Sala, M. Rossi, A. Al-Zein, S. Boseggia, E. C. Hunter, R. S. Perry, D. Prabhakaran, A. T. Boothroyd, N. B. Brookes, D. F. McMorrow *et al.*, Phys. Rev. B **90**, 085126 (2014).

[3] H. Gretarsson, J. P. Clancy, X. Liu, J. P. Hill, E. Bozin, Y. Singh, S. Manni, P. Gegenwart, J. Kim, A. H. Said *et al.*, Phys. Rev. Lett. **110**, 076402 (2013).

[4] L. Hozoi, H. Gretarsson, J. P. Clancy, B.-G. Jeon, B. Lee, K. H. Kim, V. Yushankhai, P. Fulde, D. Casa, T. Gog *et al.*, Phys. Rev. B **89**, 115111 (2014).
[5] M. M. Sala, K. Ohgushi, A. Al-Zein, Y. Hirata, G. Monaco, and M. Krisch, Phys. Rev. Lett. **112**, 176402 (2014).
[6] W. Witczak-Krempa, G. Chen, Y. B. Kim, and L. Balents, Annu. Rev. Condens. Matter Phys. **5**, 57 (2014).
[7] G. Jackeli and G. Khaliullin, Phys. Rev. Lett. **102**, 017205 (2009).
[8] T. N. Nguyen and H.-C. zur Loye, J. Solid State Chem. **117**, 300 (1995).
[9] D. Flahaut, S. Hébert, A. Maignan, V. Hardy, C. Martin, M. Hervieu, M. Costes, B. Raquet, and J. M. Broto, Eur. Phys. J. B: Condens. Matter **35**, 317 (2003).
[10] D. Mikhailova, B. Schwarz, A. Senyshyn, A. M. T. Bell, Y. Skourski, H. Ehrenberg, A. A. Tsirlin, S. Agrestini, M. Rotter, P. Reichel *et al.*, Phys. Rev. B **86**, 134409 (2012).
[11] E. Lefrançois, L. C. Chapon, V. Simonet, P. Lejay, D. Khalyavin, S. Rayaprol, E. V. Sampathkumaran, R. Ballou, and D. T. Adroja, Phys. Rev. B **90**, 014408 (2014).
[12] J. Singleton, J. W. Kim, C. V. Topping, A. Hansen, E.-D. Mun, S. Ghannadzadeh, P. Goddard, X. Luo, Y. S. Oh, S.-W. Cheong *et al.*, arXiv:1408.0758.
[13] S. Sarkar, S. Kanungo, and T. Saha-Dasgupta, Phys. Rev. B **82**, 235122 (2010).
[14] G. R. Zhang, X. L. Zhang, T. Jia, Z. Zeng, and H. Q. Lin, J. Appl. Phys. **107**, 09E120 (2010).
[15] X. Ou and H. Wu, Sci. Rep. **4**, 4609 (2014).
[16] X. Liu, V. M. Katukuri, L. Hozoi, W.-G. Yin, M. P. M. Dean, M. H. Upton, J. Kim, D. Casa, A. Said, T. Gog *et al.*, Phys. Rev. Lett. **109**, 157401 (2012).
[17] W.-G. Yin, X. Liu, A. M. Tsvelik, M. P. M. Dean, M. H. Upton, J. Kim, D. Casa, A. Said, T. Gog, T. F. Qi *et al.*, Phys. Rev. Lett. **111**, 057202 (2013).
[18] M. M. Sala, C. Henriquet, L. Simonelli, R. Verbeni, and G. Monaco, J. Electron Spectrosc. Relat. Phenom. **188**, 150 (2013).
[19] J. Kim, D. Casa, M. H. Upton, T. Gog, Y.-J. Kim, J. F. Mitchell, M. van Veenendaal, M. Daghofer, J. van den Brink, G. Khaliullin *et al.*, Phys. Rev. Lett. **108**, 177003 (2012).
[20] J. Kim, A. H. Said, D. Casa, M. H. Upton, T. Gog, M. Daghofer, G. Jackeli, J. van den Brink, G. Khaliullin, and B. J. Kim, Phys. Rev. Lett. **109**, 157402 (2012).
[21] L. J. P. Ament, G. Khaliullin, and J. van den Brink, Phys. Rev. B **84**, 020403 (2011).
[22] M. Moretti Sala, S. Boseggia, D. F. McMorrow, and G. Monaco, Phys. Rev. Lett. **112**, 026403 (2014).
[23] See Supplemental Material at http://link.aps.org/supplemental/10.1103/PhysRevB.93.224401 for more information on the *ab initio*, spin-wave, and Monte Carlo calculations, estimation of the interchain coupling, and magnetization measurements.
[24] V. M. Katukuri, H. Stoll, J. van den Brink, and L. Hozoi, Phys. Rev. B **85**, 220402 (2012).
[25] F. Aquilante, L. De Vico, N. Ferre, G. Ghigo, P.-A. Malmqvist, P. Neogrady, T. Pedersen, M. Pitonak, M. Reiher, B. Roos *et al.*, J. Comput. Chem. **31**, 224 (2010).
[26] S. Toth, W. Wu, D. T. Adroja, S. Rayaprol, and E. V. Sampathkumaran, arXiv:1604.06569.
[27] S. Chattopadhyay, D. Jain, V. Ganesan, S. Giri, and S. Majumdar, Phys. Rev. B **82**, 094431 (2010).
[28] L. Qiang, G.-H. Liu, and G.-S. Tian, Int. J. Mod. Phys. B **29**, 1550070 (2015).